

Track Finding Efficiency in *BABAR*

T. Allmendinger^a, B. Bhuyan^b, D. N. Brown^c, H. Choi^d, S. Christ^e, R. Covarelli^f, M. Davier^g, A. G. Denig^h,
M. Fritsch^h, A. Hafner^h, R. Kowalewski^d, O. Longⁱ, A. M. Lutz^g, M. Martinelli^j, D. R. Muller^k, I. M. Nugent^d,
D. Lopes Pegna^l, M. V. Purohit^m, E. Prencipe^h, J. M. Roney^d, G. Simiⁿ, E. P. Solodov^o, A. V. Telnov^l, E. Varnes^l,
R. Waldi^e, W. F. Wang^p, R. M. White^m

^aOhio State University, Columbus, Ohio 43210, USA

^bIndian Institute of Technology Guwahati, Assam, 781 039, India

^cLawrence Berkeley National Laboratory and University of California, Berkeley, California 94720, USA

^dUniversity of Victoria, Victoria, BC, V8W 3P6, Canada

^eUniversität Rostock, D-18051 Rostock, Germany

^fINFN Sezione di Perugia, Dipartimento di Fisica, Università di Perugia, I-06100 Perugia, Italy

^gLaboratoire de l'Accélérateur Linéaire, IN2P3/CNRS et Université Paris-Sud 11, Centre Scientifique d'Orsay, B. P. 34, F-91898 Orsay Cedex, France

^hJohannes Gutenberg-Universität Mainz, Institut für Kernphysik, D-55099 Mainz, Germany

ⁱUniversity of California at Riverside, Riverside, California 92521, USA

^jINFN Sezione di Bari, I-70126 Bari, Italy

^kSLAC National Accelerator Laboratory, Stanford, California 94309 USA

^lPrinceton University, Princeton, New Jersey 08544, USA

^mUniversity of South Carolina, Columbia, South Carolina, 29208, USA

ⁿUniversità di Padova, I-35131 Padova, Italy

^oBudker Institute of Nuclear Physics, Novosibirsk 630090, Russia

^pUniversity of Notre Dame, Notre Dame, Indiana 46556, USA

Abstract

We describe several studies to measure the charged track reconstruction efficiency and asymmetry of the *BABAR* detector. The first two studies measure the tracking efficiency of a charged particle using τ and initial state radiation decays. The third uses the τ decays to study the asymmetry in tracking, the fourth measures the tracking efficiency for low momentum tracks, and the last measures the reconstruction efficiency of K_S^0 particles. The first section also examines the stability of the measurements vs *BABAR* running periods.

Keywords: *BABAR*, tracking, efficiency

1. Introduction

The *BABAR* experiment operated from 1999 to 2008 at the PEP-II asymmetric e^+e^- collider at the SLAC National Accelerator Laboratory. *BABAR* was designed to study CP violation and other rare decays in flavor physics from events produced at or near the Υ resonances, from 9.46 GeV to over 11 GeV. A critical requirement for meeting *BABAR*'s science goals was the ability to efficiently and accurately detect stable charged particles, or *tracks*, produced in e^+e^- collisions. Many

analyses performed at *BABAR* require a precise estimate of the track finding efficiency, as input for measuring the absolute or relative rate of the physics process being studied.

In this paper, we present the algorithms and methods used in *BABAR* to estimate the track finding efficiency. To cover the range of particle momenta and production environments relevant to most *BABAR* analyses, a number of methods are used. To compute the tracking efficiency from data alone, these methods rely on special data samples, where additional constraints can be applied. The primary efficiency result is computed using $e^+e^- \rightarrow \tau^+\tau^-$ events, which can be cleanly iso-

Email address: bhuyan@iitg.ernet.in (B. Bhuyan)

lated in the *BABAR* data sample, and which have a simple topology. To cross-check this result, we independently measure the tracking efficiency using radiative $e^+e^- \rightarrow \pi^+\pi^-\pi^+\pi^-\gamma_{ISR}$ events, where γ_{ISR} is an initial state radiation (ISR) photon, which can be constrained kinematically. To study the reconstruction efficiency of low momentum tracks, we use $D^{*\pm} \rightarrow D^0\pi^\pm$ decays. We also present a dedicated study of the efficiency to reconstruct $K_S^0 \rightarrow \pi^+\pi^-$, whose daughter tracks can have a different efficiency due to their displacement from the primary event origin.

The strategy for the τ -based and $e^+e^- \rightarrow \pi^+\pi^-\pi^+\pi^-\gamma_{ISR}$ track reconstruction efficiency measurements is to use charge conservation and kinematics to deduce the existence of a track, given a subset of detected tracks in well-defined events. The efficiency analyses based on D^0 decays and for the K_S^0 efficiency study use a statistical approach, using properties of momentum distributions which will be described below. Systematic errors are estimated using internal self-consistency measures and by comparing different efficiency analysis techniques.

The *BABAR* detector geometry, material, and sensor response functions have been accurately modeled in a detailed simulation based on the Geant4 [1] framework. The output of the *BABAR* simulation is processed using the same reconstruction algorithms as applied to data, and the results have been found to be very similar to what we see in data. By using accurate computer models of the physics processes relevant at *BABAR* energies [2, 3], we are able to generate equivalent samples of simulated data as used in nearly all *BABAR* analyses, including the tracking efficiency analysis. *BABAR* has therefore adopted the strategy of estimating the tracking efficiency relative to that observed in the simulation, which simplifies the application of the tracking efficiency results in analysis. As will be shown in the following sections, for most of the studies, the tracking efficiency found in data agrees within errors with the efficiency found in simulated data. This allows the result of the tracking efficiency measurement to be used in analysis simply by propagating the appropriate systematic errors on the tracks involved to the simulation estimate of the analysis signal reconstruction efficiency. This strategy has been used in many scientific *BABAR* publications. However, for analyses involving a K_S^0 , a correction is required in the MC for its daughter reconstruction efficiency which depends on the kinematics of the decay of interest.

2. *BABAR* Detector and Data Sample

The *BABAR* detector is a multi-purpose device designed to simultaneously measure many properties of the multiple particles produced in e^+e^- collisions near the Υ resonances, as described in detail in [4]. Charged particles are identified in a Silicon Vertex Tracker (SVT), and a Drift Chamber (DCH), which are surrounded by a superconducting solenoid that generates an approximately uniform 1.5 Tesla magnetic field inside the sensitive volumes of these detectors.

The SVT consists of five layers of double-sided silicon strip detectors covering the full azimuthal range and the laboratory frame polar angle (θ_{lab}) range $20.1^\circ < \theta_{lab} < 150.2^\circ$ [4]. The intrinsic resolution of individual SVT position measurements of particles which traverse it varies between $10\ \mu\text{m}$ and $30\ \mu\text{m}$, depending on the incident particle direction and the readout view. The DCH consists of 7,104 hexagonal drift cells, which are approximately 1.9 cm-wide and 1.2 cm-high, made up of one sense wire surrounded by six field wires. The sense wires are $20\ \mu\text{m}$ gold-plated tungsten-rhenium, the field wires are $120\ \mu\text{m}$ and $80\ \mu\text{m}$ gold-plated aluminium. The cells are arranged in 40 cylindrical layers and the layers are grouped by four into ten *superlayers* extending from roughly 25 cm to 80 cm in the transverse direction, with full coverage over the range $24.8^\circ < \theta_{lab} < 141.4^\circ$, and partial coverage over the range $17.2^\circ < \theta_{lab} < 152.6^\circ$. The intrinsic resolution of individual measurements of track position in the DCH varies between $100\ \mu\text{m}$ and $200\ \mu\text{m}$, depending on the track position and angle relative to the wire, with an average resolution of $150\ \mu\text{m}$.

The *BABAR* detector includes a dedicated charged particle identification (PID) device based on detection of internally reflected Cherenkov radiation (DIRC), and a Cesium-iodide crystal electromagnetic calorimeter (EMC) for identifying electrons and photons. The steel for the solenoid magnet flux return is instrumented with position-sensitive chambers, which produce distinctive signatures from passing muons and pions. *BABAR* estimates the species of charged particles using a combination of information from these devices, plus the specific ionization (dE/dx) measured in both the SVT and DCH. By studying the response of these systems to high-purity control samples, likelihood functions describing a track's consistency with each of the 5 charged particle species ($e^\pm, \mu^\pm, \pi^\pm, K^\pm$, and p^\pm) directly observable in the *BABAR* tracking system are defined. Samples of specific particle species of varying efficiency and purity are selected by cutting on appropriate likelihood ratios.

The results presented in this paper are based on the full *BABAR* data sample, collected in seven distinct periods, Runs 1-7. Runs 1-6 correspond to data collected with a center-of-mass (CM) collision energy near or at the $\Upsilon(4S)$ resonance and Run 7 corresponds to the data collected with a CM collision energy at the $\Upsilon(3S)$ and $\Upsilon(2S)$ resonances.

3. *BABAR* Track Reconstruction Algorithms

Tracks are reconstructed in *BABAR* using a combination of several algorithms. Tracks with transverse momentum above roughly 150 MeV/c are principally found in the DCH. Track *segments* are identified as contiguous sets of hits in a super-layer having a pattern consistent with coming from a roughly radial track. Segments are linked using their position and angle to form a track candidate. Track candidates are fit to a helix, which is used to resolve the left-right ambiguity, and to remove *outlier* hits. The candidate is kept if at least 20 DCH hits remain. Tracks with large impact parameter are found in the DCH using a less restrictive algorithm. Tracks found in the DCH are fit using a Kalman filter [5] fit, which accounts for material effects and corrects for magnetic field inhomogeneities. The Kalman filter track fit is extrapolated inwards, and SVT hits consistent with the extrapolated track position and covariance are added.

Tracks with low transverse momentum are found principally in the SVT using hits not already associated with tracks found in the DCH. Sets of four or more ϕ hits (which measure the position in the plane transverse to the beam direction), in different layers of the SVT and consistent with lying on a circle, are selected. Hits in the orthogonal (z) view of the same wafers as the ϕ hits are then added to form three-dimensional track candidates. Candidates with at least 8 hits are selected, and fit using the Kalman filter. Additional tracks are found in the SVT using space points constructed from pairs of ϕ and z hits not already used in other tracks. Sets of at least 4 space points consistent with a helix fit are selected as tracks. DCH hits are added to tracks found in the SVT in a procedure analogous to how SVT hits are added to tracks found in the DCH.

After all the tracks in an event are found, they are filtered to remove duplicate tracks due to hard scattering in the material separating the SVT and the DCH, decays in flight, or pattern recognition errors in the DCH, where stereo and axial hits generated by a single particle are sometimes reconstructed as separate tracks. A final pass to remove inconsistent hits and to add individual

hits missed in the pattern recognition is then performed using the Kalman filter fit.

The resultant set of tracks is referred to as *Charged Tracks* (CT). A *Good Tracks* (GT) subset of tracks, with a higher probability of originating from the primary e^+e^- interaction, is selected from these. The GT selection requires the impact parameter with respect to the average interaction point be less than 1.5 cm in the transverse direction, and less than 2.5 cm along the magnetic field (z) direction. Analyses at *BABAR* generally use either the CT or the GT track selection, and the tracking efficiency studies described in this note are performed independently for both.

4. Tau31 Tracking Efficiency Study

The efficiency of charged track reconstruction at *BABAR* is determined using $e^+e^- \rightarrow \tau^+\tau^-$ events. With over 430 million τ pair events collected at *BABAR*, τ decays provide an opportunity to make a precision measurement of the tracking efficiency. At the CM energies produced at *BABAR*, τ decays are an ideal candidate for measuring the tracking efficiency because they have a momentum and angular distributions of tracks that are similar to those from decays of D and B mesons. Decays of τ leptons have a high track density due to the initial boost, $\beta \sim 0.94c$, of the τ leptons, while the total track multiplicity is low. The τ lepton has a life-time of $(290.6 \pm 1.0) \times 10^{-15}s$, which results in a transverse flight length of 200 μm at the *BABAR* CM energies, a value that is slightly larger than the beam spot size but small enough not to impact the tracking efficiency.

The tracking efficiency is measured using $e^+e^- \rightarrow \tau^+\tau^-$ events in which one τ lepton decays leptonically via $\tau^\pm \rightarrow \mu^\pm \nu_\mu \nu_\tau$, and the other τ lepton decays semi-leptonically to 3 charged hadrons via $\tau^\mp \rightarrow h^\mp h^\mp h^\pm \nu_\tau + \geq 0$ neutrals (excluding K^0), referred to as *Tau31* events. The tracking efficiency is measured using the 3-prong τ decays. The branching ratio of $\tau^\pm \rightarrow \mu^\pm \nu_\mu \nu_\tau$ and 3-prong τ decays are $(17.36 \pm 0.05)\%$ and $(14.56 \pm 0.08)\%$ [6] respectively, so that *Tau31* events constitute over 5% of the total. The τ pair candidates are selected by requiring an isolated muon track, plus at least two other reconstructed tracks consistent with being hadrons. Events are selected in two overlapping channels; those where two of the hadrons have the same charge (“same-sign”), and those where two of the hadrons have opposite charge (“opposite-sign”). Requiring a muon track is an essential part of suppressing non- τ backgrounds: radiative Bhabha events where the photon interacts with the detector material producing an e^+e^- pair (conversion), $\gamma\text{-}\gamma$ events, and $q\bar{q}$ events.

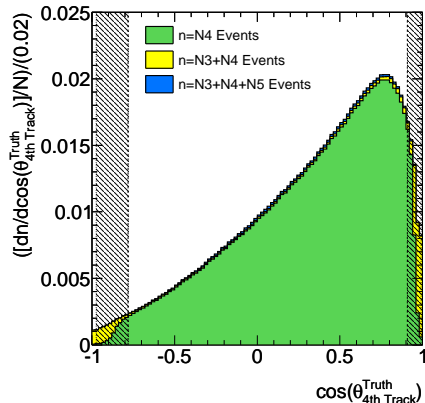


Figure 1: The true $\cos(\theta)$ in the laboratory frame for the fourth track for the selected opposite-sign and same-sign MC events. $N = N_3 + N_4 + N_5$ is the number of selected same-sign and opposite-sign events. N_4 is the number of events where the fourth track is found for the CT definition, N_3 is the number of events where the fourth track is not found for the CT definition and N_5 is the number of events where two CT candidates are found for the fourth track. The dotted lines indicate the outer edge of the tracking detectors, while the dashed lines indicate the edge where the full detector coverage begins. The region in between where there is partial coverage is indicated by the shading.

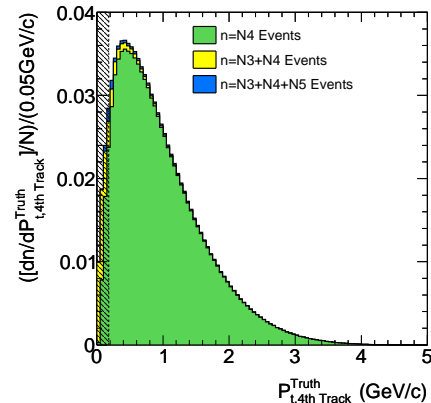


Figure 2: The true p_t for the fourth track for the selected opposite-sign and same-sign MC events. $N = N_3 + N_4 + N_5$ is the number of selected same-sign and opposite-sign events, N_4 is the number of events where the fourth track is found for the CT definition, N_3 is the number of events where the fourth track is not found for the CT definition and N_5 is the number of events where two CT candidates are found for the fourth track. The tracks in the shaded region do not reach the outer edge of the DCH.

223 Charge conservation infers the existence of the fourth
224 track.

225 The tracking efficiency ϵ is defined by

$$\epsilon \times A = \frac{N_4}{N_3 + N_4} \quad (1)$$

226 where A is the geometric acceptance of the fourth track
227 constrained by the τ pair kinematics and the selection
228 criteria of the Tau31 sample, N_4 is the number of events
229 where the fourth track is found, and N_3 is the number
230 of events where the fourth track is not found. The geo-
231 metric acceptance of the *BABAR* detector for a uniform
232 $\cos(\theta)$ distribution is $\sim 83\%$. In figures 1 and 2, the
233 geometric acceptance of the detector is plotted for simu-
234 lated events as a function of the polar angle (θ) and the
235 transverse momentum (p_t) of the fourth track, respec-
236 tively. These figures demonstrate the limited angular
237 acceptance of the detector, and the poor acceptance for
238 low momentum tracks.

239 4.1. Monte Carlo Samples

240 $\tau^+\tau^-$ pair events are simulated with higher-order ra-
241 diative corrections using the KK2f Monte Carlo (MC)
242 generator [7] with τ decays simulated with Tauo1a [8,
243 9]. The simulated Standard Model backgrounds in-
244 clude: $b\bar{b}$; $c\bar{c}$; $s\bar{s}$; $u\bar{u}$; and $\mu^+\mu^-$ events [3, 7, 8, 9, 10].

245
246
247
248
249
250
251

The number of simulated background events is compa-
rable to the number expected in the data, with the ex-
ception of Bhabha and two-photon events, which are not
simulated. Bhabha and two-photon events backgrounds
are studied with control samples. The detector simula-
tion and reconstruction of the MC events is described in
Section 2.

252 4.2. Event Selection

253
254
255
256
257
258
259
260
261
262
263
264
265
266
267
268
269
270
271
272

We require the events to have a minimum of three GT
and a maximum of five CT tracks. Events with K_s^0 are
removed, where the K_s^0 candidate is defined as having
two oppositely charged tracks with an invariant mass
within 10 MeV of the K_s^0 mass [6], a vertex displaced
more than 2 mm from the beam-spot and a vertex fit χ^2
probability of more than 1%. The three GT tracks are
required to have $p_t > 100$ MeV. To remove any remain-
ing duplicate tracks, the three GT tracks are required to
satisfy an isolation cut in θ , ϕ and momentum by 0.1
rad, 0.1 rad and 0.4 GeV, respectively. One of the three
GT tracks must be more than 120 degrees from the other
track. This isolated track must satisfy a tight muon PID
selection. At least two of the other tracks are required
to be identified as pions, by being inconsistent with a
loose electron PID selection.

For the “same-sign” channel ($\tau^\pm \rightarrow \pi^\pm \pi^\pm X^\mp \nu_\tau$, where
 X^\mp is the unidentified 4th track), we require $0.3 \text{ GeV} < M_{\pi^\pm \pi^\pm} < M_\tau$ to ensure that the charged pions are
consistent with coming from a τ lepton decay. For the

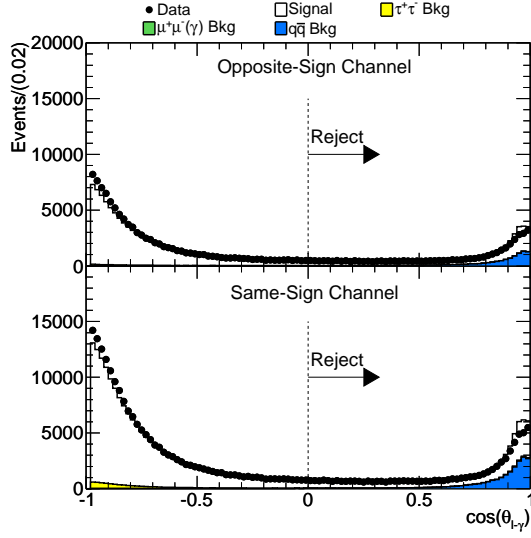


Figure 3: The cosine of the angle between the muon and the closest identified photon ($\cos(\theta_{\mu\gamma})$) with all other selection criteria applied for about 15% of the *BABAR* data sample. The points represent the data, the empty histogram represents the 3 prong τ decays, the light shaded histogram represents the other $\tau^+\tau^-$ MC, the medium dark histogram represent the $\mu^+\mu^-$ MC and the dark histogram represents the $q\bar{q}$ MC. The background contamination in these samples is small.

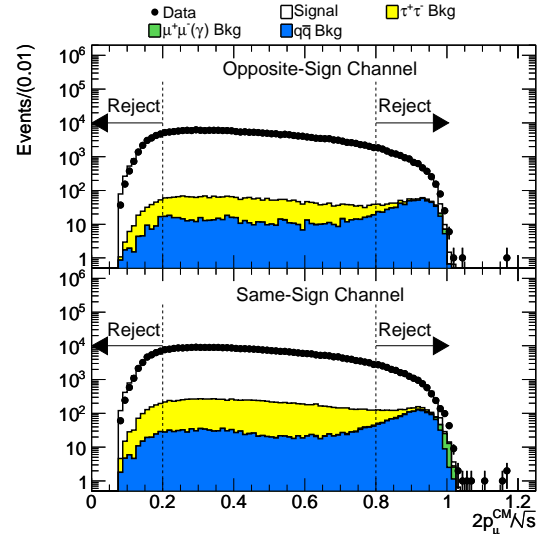


Figure 4: The $2p_{\mu}^{CM} / \sqrt{s}$ of the tag track with all other selection criteria applied for about 15% of the *BABAR* data sample. Contamination from di-muon and Bhabha events, which peak at $2P / \sqrt{s} = 1.0$, are negligible. The points represent the data, the empty histogram represents the 3 prong τ decays, the light shaded histogram represents the other $\tau^+\tau^-$ MC, the medium dark histogram represent the $\mu^+\mu^-$ MC and the dark histogram represents the $q\bar{q}$ MC.

273 “opposite-sign” channel ($\tau^{\pm} \rightarrow \pi^{\pm}\pi^{\mp}X^{\pm}\nu_{\tau}$), we require
 274 $|M_{\pi^{\pm}\pi^{\mp}} - M_{\rho}| < 100$ MeV to ensure that the charged pions
 275 are consistent with coming from a ρ meson. This produces a loose selection for the “same-sign” channel
 276 and a tight selection for the “opposite-sign” channel. An event can be selected in either or both channels. In the
 277 case where more than one same-sign or opposite-sign pion pairing is possible, the pair with the highest laboratory
 278 frame p_t is selected.

282 To remove $q\bar{q}$ backgrounds, events with neutral particles with an energy greater than 0.5 GeV that are within
 283 90 degrees from the muon track are removed. Figure 3 shows the cosine of the angle between the muon and the
 284 photon ($\cos(\theta_{\mu\gamma})$). To suppress radiative di-muon and Bhabha backgrounds with conversions, the muon track
 285 must have a CM momentum, (p_{μ}^{CM}) less than 80% and greater than 20% of $\sqrt{s}/2$, where \sqrt{s} is the beam CM
 286 energy. To further reduce the non- τ backgrounds, the polar angle of the system of charged particles, the μ - $\pi\pi$
 287 system, in the CM frame must satisfy $|\cos(\theta_{\mu-\pi\pi})| < 0.8$, with the net transverse momentum of the μ - $\pi\pi$ system
 288 being more than 0.3 GeV.

289 After the same-sign and opposite-sign events have been selected, fourth track candidates are selected,
 290 which are required to have the appropriate charge to come from a τ pair event and satisfy the track defini-
 291
 292
 293
 294
 295
 296
 297
 298

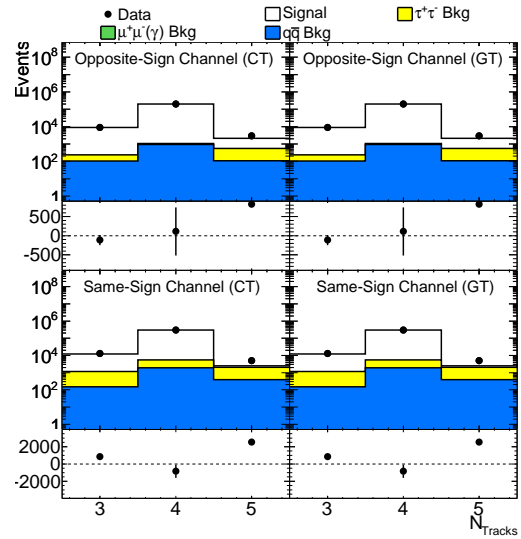


Figure 5: The track multiplicity in events that have been selected with the same-sign or opposite-sign selection presented using the CT and GT definitions of the fourth track with all criteria applied for about 15% of the *BABAR* data sample. The points represent the data; the contributions from different backgrounds are shown in the histograms.

tions being studied. Figure 5 shows the multiplicity of the selected same-sign and opposite-sign events for the CT and GT definitions. Once the fourth track candidates have been selected, the tracking efficiency is determined by using Eq. 1. The difference in the tracking efficiency between data and MC is defined using Eq. 2.

$$\Delta = 1 - \frac{\epsilon_{MC}}{\epsilon_{data}}. \quad (2)$$

Similarly, the charge asymmetry of the tracking efficiency is defined using Eq. 3.

$$a_{\pm} = \frac{\epsilon_{+} - \epsilon_{-}}{\epsilon_{+} + \epsilon_{-}}. \quad (3)$$

where the efficiency measurements in Eq. 2 and Eq. 3 also include the detector acceptance.

Monte Carlo studies indicate that the backgrounds that could potentially bias the determination of the relative tracking efficiency and the charge asymmetry are: events with two primary tracks from the $e^{+}e^{-}$ collision and a photon that converts into an electron pair; $q\bar{q}$ and τ pair events with six tracks; and $\tau^{-} \rightarrow \pi^{-}K_s^0\nu_{\tau}$ where the K_s^0 decays into a $\pi^{-}\pi^{+}$ pair with a vertex that deviates significantly from the primary vertex. For the background events with conversions and K_s^0 , the reconstruction efficiency could differ from that of tracks originating from the interaction point of the $e^{+}e^{-}$ collision. The largest source of conversions comes from hadronic τ decays with one charged track and 1 or more neutral particles. This includes $\tau^{\mp} \rightarrow \rho^{\mp}\nu_{\tau}$ and $\tau^{\mp} \rightarrow h^{\pm}\pi^0\nu_{\tau}$ ($h = \pi$ or K), which have branching fractions of $(25.51 \pm 0.09)\%$ and $(9.51 \pm 0.11)\%$ [6] respectively. The contribution from the τ decays with a K_s^0 is small due to the suppression by the selection cuts and the branching fractions. The largest background from events with six tracks originating from the $e^{+}e^{-}$ collision is from $\tau^{\pm} \rightarrow \mu^{\pm}\nu_{\mu}\nu_{\tau}$, $\tau^{\mp} \rightarrow h^{\mp}h^{\mp}h^{\mp}h^{\pm}h^{\pm} \geq 0$ neutrals ν_{τ} (excluding K_s^0) events which have a branching fraction of $(0.102 \pm 0.004)\%$. The contamination from τ pair events with six tracks is $\ll 0.1\%$ for both the same-sign and opposite-sign channels.

4.3. Systematic Uncertainties

The primary systematic uncertainties in measuring the tracking efficiency and charge asymmetry arise due to mis-modeling of background contamination, which can bias the tracking efficiency due to fake tracks. The largest background comes from events with two tracks and a photon that converts in the detector material producing an $e^{+}e^{-}$ pair. This background includes contributions from τ pair events, radiative di-muon, Bhabha events, and two-photon events.

We estimate the effect of background mis-modeling on the efficiency measurement using control samples selected to be enriched in photon conversion backgrounds. The control samples are selected using the standard selection, minus the vertex requirements, the loose electron rejection using PID, and the same-sign and opposite sign invariant mass cuts. Instead of these we apply a tight electron PID selection to two oppositely charged tracks. The invariant mass of the two oppositely charged tracks is required to be less than 0.1 GeV using an electron mass hypothesis. The agreement between the data and MC for the selection efficiency of this control sample is taken as the uncertainty on the modeling of conversions. This is propagated to the Δ and the charge asymmetry measurements using the measured rates. Note that this systematic error includes both contributions from the mis-modeling of the conversions, and contributions from backgrounds that are not included in the MC simulation.

To assess the impact of potentially different track multiplicity from $q\bar{q}$ backgrounds and the small contribution from τ decays with a K_s^0 , the efficiency difference Δ and the charge asymmetry are calculated without subtracting these backgrounds. The difference between these and the nominal values computed after background subtraction is conservatively taken as the systematic uncertainty.

To account for possible differences in the rate of fake tracks, a systematic uncertainty based on the difference between Δ and the charge asymmetry calculated with (ϵA) and

$$\epsilon' \times A = \frac{N_4}{N_3 + N_4 + N_5} \quad (4)$$

is included, where N_5 is the number of events where two candidate fourth tracks are found.

As a cross check on the systematic errors, we compute Δ and the charge asymmetry, a_{\pm} , separately in the same-sign and opposite-sign channels, and find these to be consistent within statistical and background uncertainties.

In general, tracks selected in an analysis will not have the same kinematic distributions as the tracks in the Tau31 study. Therefore, when applying the efficiency results of the Tau31 study to an analysis, an additional systematic uncertainty is needed to account for the efficiency dependence on track kinematics. In the Tau31 analysis we do not estimate the dependence of tracking efficiency on track density or track multiplicity. That is done in the ISR analysis presented in Section 5.

We quantify the kinematic variation in Δ and the charge asymmetry by measuring them as a function of fourth track polar angle θ and transverse momentum p_T .

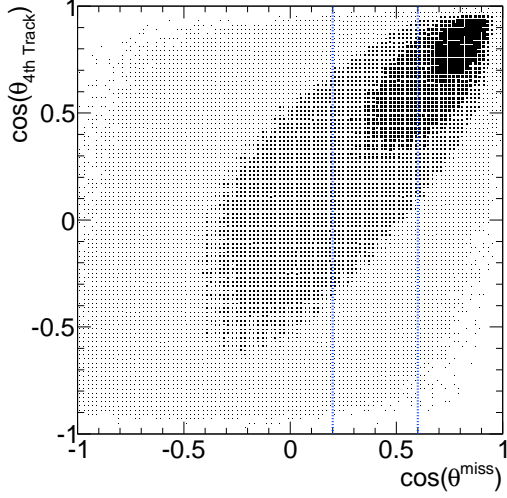


Figure 6: The $\cos(\theta_{4th\ Track})$ as a function of the $\cos(\theta^{miss})$ for data events in Runs 1-6 selected with the same-sign and opposite-sign selection criteria. The fourth track is identified using the CT definition. The dotted lines indicate the boundaries of the $\cos(\theta^{miss})$ regions selected for determining the systematic uncertainty on Δ and the charge asymmetry as a function $\cos(\theta_{4th\ Track})$.

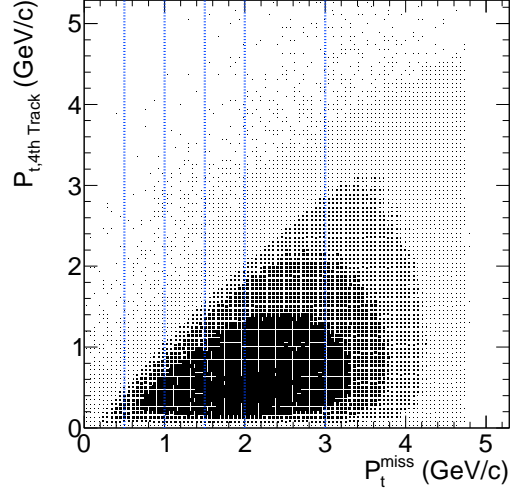


Figure 7: The $P_{t,4th\ Track}$ as a function of the P_t^{miss} for data events in Runs 1-6 selected with the same-sign and opposite-sign selection criteria. The fourth track is identified using the CT definition. The dotted lines indicate the boundaries of the P_t^{miss} regions selected for determining the systematic uncertainty on Δ and the charge asymmetry as a function $P_{t,4th\ Track}$.

Because of the three missing neutrinos in the event, θ and p_t of the fourth track cannot be exactly determined. We therefore construct estimators based on the trajectories of the muon and two identified pions, and use them to define different kinematic regions. We define the $\cos(\theta)$ estimator to be

$$\cos(\theta^{miss}) = \cos(\theta_{\pi_1\pi_2}), \quad (5)$$

where the $\pi_1\pi_2$ system is defined as the vector sum of the two identified pions. The correlation between the $\cos(\theta^{miss})$ estimator and the $\cos(\theta_{4th\ Track})$ is shown in Figure 6.

For p_t we define the estimator as

$$p_t^{miss} = \sqrt{\left(\frac{\sqrt{s}}{2} - E_{\pi_1} - E_{\pi_2}\right)^2 - m_\pi^2} \times \cos(\theta^{miss}), \quad (6)$$

where \sqrt{s} is the beam energy, E_{π_1} is the energy of the i th identified pion and m_π is the mass of a pion. The correlation between the p_t^{miss} and $P_{t,4th\ Track}$ is shown in Figure 7.

The systematic uncertainty on Δ and the charge asymmetry as a function of the estimated $\cos(\theta)$ and p_t is defined as the RMS = $\sqrt{\sum_i^n (\Delta/a_{\pm} - \Delta_i/a_{\pm,i})^2 / (n-1)}$, where n is the number of regions, Δ/a_{\pm} is the average Δ or charge asymmetry as defined previously, and $\Delta_i/a_{\pm,i}$

is the Δ or the charge asymmetry in the i th region selected with the estimator. The systematic uncertainty due to P_t and θ dependence is quantified in Table 1.

Table 1: Systematic uncertainties for Δ in P_t and θ . The P_t and θ uncertainty in the $\mathcal{Y}(2s)$ and $\mathcal{Y}(3s)$ runs are sensitive to the limited statistics.

Data Period	P_t Uncertainty	θ Uncertainty
GTL Track Definition		
Runs 1-6	0.20%	0.11%
Run 7 - $\mathcal{Y}(2s)$	0.30%	0.38%
Run 7 - $\mathcal{Y}(3s)$	0.80%	0.42%
CT Track Definition		
Runs 1-6	0.10%	0.06%
Run 7 - $\mathcal{Y}(2s)$	0.65%	0.28%
Run 7 - $\mathcal{Y}(3s)$	0.79%	0.32%

4.4. Tau31 Results vs. Run Period

Figure 8 shows the run-by-run tracking efficiency for the two track definitions studied in this analysis: GT and CT. The tracking efficiencies in the data and MC are found to be consistent with each other. This can be seen in Figure 9 which presents Δ . The charge asymmetry can be seen in Figure 10. The plots suggest that there is no significant charge bias in the tracking efficiency.

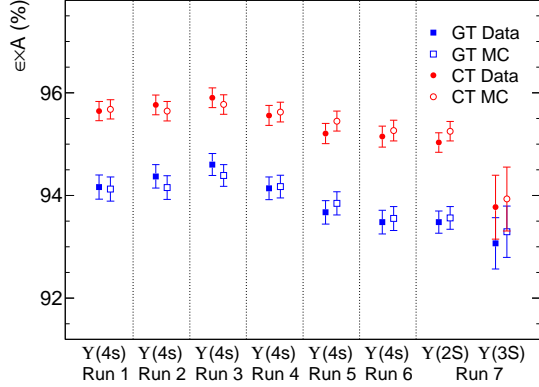


Figure 8: The tracking efficiency as a function of run number for the GT definition (top) and the CT definition (bottom). The data are represented by solid markers and the MC by open markers. The error bars represent the total uncertainty where the statistical and background systematic uncertainties have been added in quadrature.

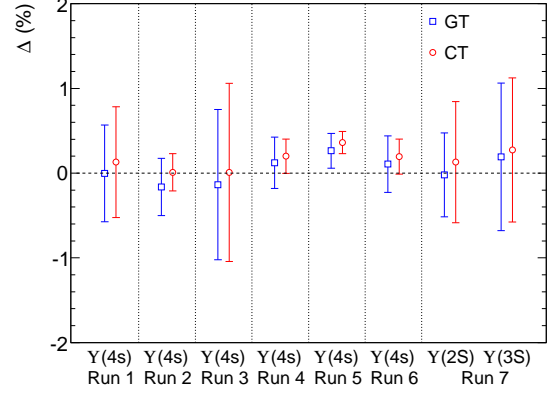


Figure 9: The data-MC difference in the tracking efficiency as a function of run number for the GT definition and the CT definition. The error bars represent the total uncertainty where the statistical and systematic uncertainties have been added in quadrature.

411 The stability of the agreement between data and MC
 412 over the 7 run periods (as shown in Figures 9 and 10)
 413 demonstrates that the detector simulation, which is up-
 414 dated regularly, accurately models the tracking perfor-
 415 mance of the detector as a function of time. Because
 416 there is no significant time variation observed between
 417 Runs 1 and 6 in Δ and in the charge asymmetry of the
 418 tracking efficiencies, an average of Runs 1-6 for Δ and
 419 the charge asymmetry of the tracking efficiencies is cal-
 420 culated. These averages are used to calculate the sys-
 421 tematic uncertainty due to tracking efficiency. The sys-
 422 tematic uncertainty per track for a given track defini-
 423 tion is

$$\Sigma_{Tracking}^{Tau31} = \frac{\sigma_{\Delta CT/GT}}{1 - \Delta_{CT/GT}} \quad (7)$$

424 where $\sigma_{\Delta CT/GT}$ is the total uncertainty on Δ for the given
 425 track definition. These results are the primary source of
 426 systematic uncertainty in track reconstruction efficiency
 427 in *BABAR*.

5. Tracking efficiency using the ISR channel $\pi^+\pi^-\pi^+\pi^-\gamma_{ISR}$

430 A complementary approach to the Tau31 method is
 431 to study the tracking efficiency using processes such as
 432 $e^+e^- \rightarrow \pi^+\pi^-\gamma_{ISR}$ and $e^+e^- \rightarrow \pi^+\pi^-\pi^+\pi^-\gamma_{ISR}$, where a
 433 high energetic photon γ_{ISR} is emitted from an initial lep-
 434 ton. This final state provides a clean event sample, cov-
 435 ering a wide range of momenta and polar angles of the
 436 tracks. In this section, we describe one such measure-
 437 ment involving four pions in the final state along with

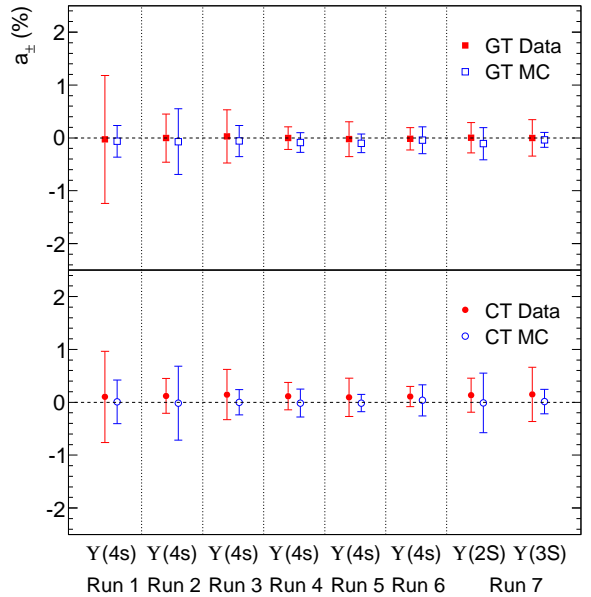


Figure 10: The charge asymmetry of the tracking efficiency as a function of run number for the GT definition (top) and the CT definition (bottom). The data are represented by the solid markers and the MC by the open markers. The error bars represent the total uncertainty where the statistical and systematic uncertainties have been added in quadrature.

the ISR photon. The Tau31 method has a higher statistical accuracy, allowing the explicit study of time dependent effects. By contrast, since no neutrinos are present in the final state, the ISR events allow a more precise estimate of the missing track parameters than the Tau31 method. In addition, the track density for ISR events is higher compared to the events in the Tau31 study, corresponding to different *BABAR* physics channels. The high track density in combination with the precise track parameter prediction allows studying the track overlap effects in tracking efficiency.

To study tracking efficiency with ISR, we use two event samples: one in which all 4 charged particles are reconstructed (4-track), and one in which only 3 charged particles are found (3-track). Using energy and momentum conservation in a kinematic fit, we can accurately predict the direction and momentum of the missing track in the 3-track sample. By calculating the ratio of the number of lost tracks $N_{lost\ tracks}$ to the number of measured tracks $N_{detected\ tracks}$, we obtain the tracking inefficiency, η , defined in equation (8), and the tracking efficiency, ϵ , according to equation (9). Both can be measured as a function of the kinematic properties of the missing track.

$$\eta = \frac{N_{lost\ tracks}}{N_{detected\ tracks} + N_{lost\ tracks}} \quad (8)$$

$$\epsilon = 1 - \eta \quad (9)$$

5.1. ISR Event Selection

For the ISR efficiency measurement we require that the tracks have a polar angle inside the detector acceptance ($-0.82 < \cos\theta_{ch} < 0.92$), and that the transverse distance of closest approach of the track to the event vertex (or nominal interaction point if no primary event vertex is found) be smaller than 1.5 cm, and be within 2.5 cm in the beam direction. Tracks with less than 100 MeV/c transverse momentum are rejected. The ISR photon is restricted to the polar angular range inside the EMC acceptance ($0.5\text{ rad} < \theta_{ISR} < 2.4\text{ rad}$), and a minimum photon energy of $E_{ISR} > 3\text{ GeV}$ is required. Either 3 or 4 selected tracks are required in the event.

In order to suppress radiative Bhabha events, we reject events where the two most energetic tracks pass a loose electron PID selection. This also removes most $\gamma\gamma$ events with an additional high energetic photon ($E_{\gamma,cm} > 4\text{ GeV}$) in opposite direction to the ISR photon candidate. We require the minimum angle between the charged tracks and the ISR photon to be larger than 1.0 rad, which rejects a large fraction of $e^+e^- \rightarrow q\bar{q}$, ($q = u, s$) and $e^+e^- \rightarrow \tau^+\tau^-$ event backgrounds. Events

with one or two tracks with PID consistent with being a K^\pm in the 3-track or the 4-track sample are rejected, respectively. Finally, we require the 4π invariant mass to be in the range of $1.2\text{ GeV}/c^2 < M_{4\pi} < 2.4\text{ GeV}/c^2$, where we expect a high signal to noise ratio.

Backgrounds from $e^+e^- \rightarrow q\bar{q}$ ($q = u, s$) are simulated with JETSET [10], while $e^+e^- \rightarrow \tau^+\tau^-$ backgrounds are simulated using KORALB [11]. The ISR-channels are simulated with the AFKQED [12] generator, based on an early version of PHOKHARA [13]. The MC samples are normalized according to the luminosity observed in the data.

5.2. ISR Kinematic Fit

Selected events are subjected to a kinematic fit assuming the $\pi^+\pi^-\pi^+\pi^-\gamma_{ISR}$ signal hypothesis $\chi^2_{4\pi}$, as well as the $K^+K^-\pi^+\pi^-\gamma_{ISR}$ background hypothesis $\chi^2_{2K2\pi}$. The fit in the 4-track (3-track) sample uses the four (three) tracks, the ISR photon and the kinematic information of incoming electron and positron. Energy and momentum conservation leads to four (one) constraints, or a 4C-fit (1C-fit), respectively.

The resulting χ^2 distributions are shown in Fig. 11. The χ^2 distributions are broader than expected, partly due to detector resolution effects, but mostly because additional ISR photons are not included into the kinematic fit hypothesis. In Fig. 11(a) the 4-track sample shows a good agreement between the data and MC in the presence of negligible background.

In Fig. 11(b) the corresponding χ^2 distributions are shown for the 3-track sample. Here, we also require the predicted polar angle for the missing track be in the detector acceptance ($-0.82 < \cos\theta_{ch} < 0.92$) region. The relative amount of background is much larger in this sample, since the kinematic closure that suppresses a lot of background in the 4-track sample is weaker with only one constraint. The visible difference between the number of events after background subtraction (red) and signal MC (black) suggests that more π tracks are lost in data than are described by MC.

Fig. 11(b) also shows a difference in the shape of the χ^2 distributions between the data and MC. The plateau in the background MC at large χ^2 suggests that all backgrounds are not subtracted from data. Therefore we perform an additional background subtraction based on data sidebands. The idea of the sideband subtraction is illustrated in Fig. 12, which plots the 3-track χ^2 distribution for a subset of the *BABAR* data. We define a signal region enriched in signal events, which contains N_1 events. The control region, which has substantial background contributions, contains N_2 events. Let N_{1s} (N_{1b})

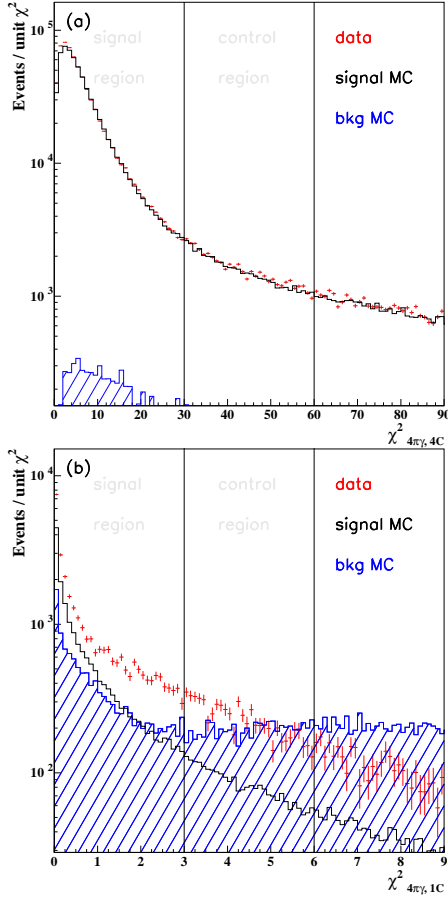


Figure 11: (a): $\chi^2_{4\pi}$ distribution for 4-track sample (4C). Data with subtracted background (red points), signal MC (black histogram) and the sum of background MC channels (blue histogram). (b): Corresponding $\chi^2_{4\pi}$ distributions for the 3-track sample (1C). The signal and control regions are indicated with vertical lines, with the region in the extreme left being the signal region and the area in the middle being the control region.

534 be the number of signal (background) events in the sig-
 535 nal region, and N_{2s} (N_{2b}) the corresponding numbers for
 536 the control region. Assuming one knows the ratios,

$$a = \frac{N_{2s}}{N_{1s}} \quad \text{and} \quad b = \frac{N_{2b}}{N_{1b}} \quad (10)$$

537 the number of signal events can then be calculated ac-
 538 cording to the following equation:

$$N_{1s} = \frac{b \cdot N_1 - N_2}{a - b} \quad (11)$$

539 We define signal and control regions in the 4-track
 540 sample as $\chi^2_{4\pi,4C} < 30$ and $30 < \chi^2_{4\pi,4C} < 60$ respec-
 541 tively. The corresponding regions in the 3-track sample
 542 are chosen so that the ratio of events in the signal to con-
 543 trol region is the same as in the 4-track sample, resulting

544 in $\chi^2_{4\pi,1C} < 3$ and $3 < \chi^2_{4\pi,1C} < 6$ respectively. The ra-
 545 tio a is determined using signal MC. In order to obtain
 546 b , we assume any difference in tracking inefficiency be-
 547 tween data and MC does not depend on $\chi^2_{4\pi}$. Therefore
 548 we performed a fit of the difference between data and
 549 MC using a linear Probability Density Function (PDF),
 550 allowing a scale-factor for MC.

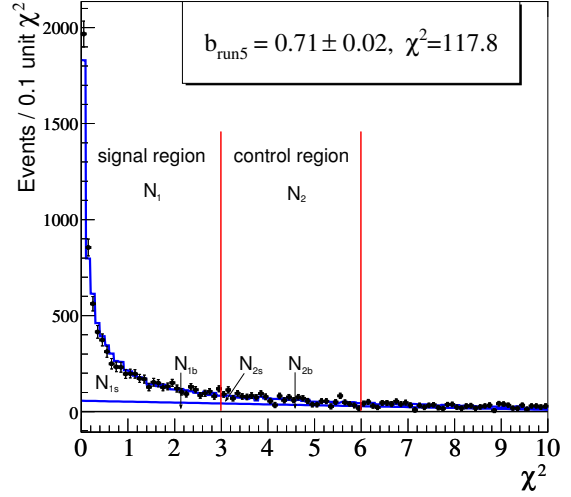


Figure 12: Fit result for sideband parameter b using Run 5 fitting signal MC (blue histogram) and a linear background (blue line) to data (black points). Also indicated are the number of signal $N_{1s/2s}$ and background $N_{1b/2b}$ events in the signal and control region.

551 The result of the fit is shown in Fig. 12. Small dis-
 552 crepancies at low χ^2 indicate that there is still some
 553 background present. The remaining difference in the χ^2
 554 distribution is consistent within the uncertainty of the
 555 cross section of the peaking background contributions
 556 that have been subtracted. After subtracting the addi-
 557 tional background using equation 11, the inefficiency
 558 difference between data and MC $\Delta\eta = \eta_{data} - \eta_{MC}$ is
 559 determined to be

$$\Delta\eta = (0.75 \pm 0.05_{stat} \pm 0.34_{syst})\%. \quad (12)$$

560 The systematic uncertainty on $\Delta\eta$ is dominated by
 561 the uncertainty of the cross section of the subtracted in-
 562 dividual background contributions in the 3-track sam-
 563 ple. Most of these cross sections have been measured
 564 in previous *BABAR* analyses [14, 15, 16, 17, 18]. The
 565 normalization of the additional contributions of contin-
 566 uum and $e^+e^- \rightarrow \tau\tau$ backgrounds have been verified
 567 with specific kinematic distributions. Note that this re-
 568 sult is not directly comparable to the Tau31 efficiency
 569 result, as that was calculated using an isolation require-

570 ment between the tracks. The effect of track overlaps is
 571 discussed in the next section.

572 5.3. ISR Efficiency Kinematic Dependence

573 In Fig. 13 the dependence of $\Delta\eta$ on the polar angle θ
 574 (a) and the transverse momentum p_t (b) of the missing
 575 track is presented. The dependence on p_t is flat within
 576 the uncertainties of 0.4%. A slight dependence on the
 577 polar angle is visible with almost no difference between
 578 data and MC in the forward region at small polar angles
 579 and a difference of approximately 1% in the central and
 580 backward region. Due to the beam energy asymmetry
 581 at *BABAR*, high energy photons are preferably emitted
 582 in the forward direction at small polar angles. In ISR
 583 events, the hadronic system is emitted back-to-back to
 584 the ISR photon. The energy of the photon is correlated
 585 with the opening angle of the cone of the hadronic sys-
 586 tem. This correlation leads to an increasing track over-
 587 lap probability in the backward region of the detector,
 588 which is not perfectly modeled by MC as shown in the
 589 following.

590 One source of tracking inefficiency is when two
 591 tracks overlap in the detector, causing sensor signals
 592 from one or both to be lost or distorted, and creating
 593 hit patterns that can be hard for the track finding al-
 594 gorithms to distinguish. *BABAR* tracking inefficiency
 595 is most affected by overlaps in azimuth, as the DCH
 596 largely projects out track polar angle. Due to magnetic
 597 bending, tracks with the same charge are more likely
 598 to overlap in azimuth than tracks with opposite charge.
 599 Furthermore, the overlap between tracks with opposite
 600 charge depends in an asymmetric way on the azimuthal
 601 angle between them. These effects are shown schemat-
 602 ically in Fig. 14. To study the dependence of tracking
 603 efficiency on overlap, we define variables sensitive to
 604 the charge-dependent two-track azimuthal separation:

605 The effect of track loss due to overlapping tracks with
 606 different charge (DC) is visible in the distribution of
 607 the charge oriented azimuthal angle difference between
 608 the lost track and the reconstructed track with different
 609 charge $\Delta\phi_{DC} = \phi(\pi^+) - \phi(\pi^-)$. Since in our study there
 610 are always two pions with the different charge of the
 611 missing pion, two angles are obtained for each event.
 612 In Fig. 15(a) the $\Delta\phi_{DC}$ distribution is plotted for data
 613 and MC. The asymmetric distribution shows that the DC
 614 tracking inefficiency peaks at small positive values.
 615

616 The number of tracks lost due to DC track over-
 617 lap is estimated by subtracting the negative half of this
 618 distribution from the positive, as illustrated for MC in
 619 Fig. 15(b). The inefficiency is corrected as indicated
 620 in equation 13, leading to a correction for overlapping
 tracks with different charge DC of 0.41%.

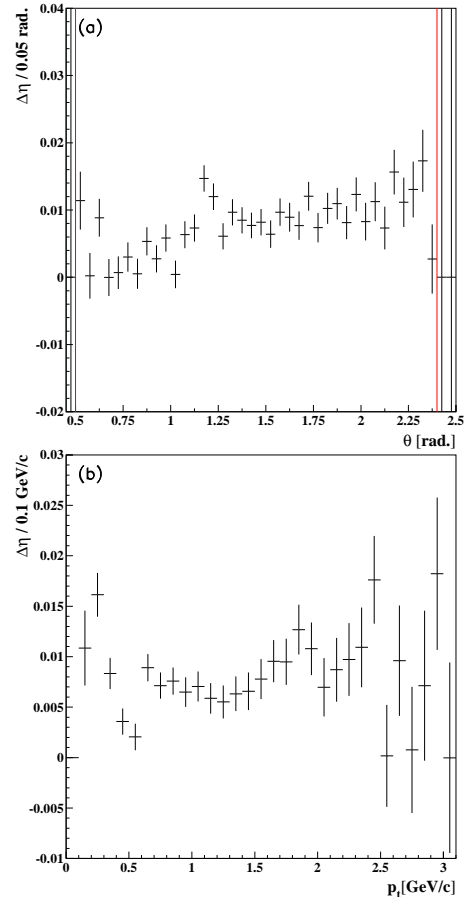


Figure 13: Relative data-MC difference of tracking inefficiency vs. the polar angle of the track θ (a) and vs. the transverse momentum p_t (b). Red lines indicate the detection region used to determine the average inefficiency.

$$\eta' = \frac{N_{\text{lost tracks}} - N_{\text{overlapping tracks}}}{N_{\text{tracks}}} \quad (13)$$

We describe the same charge (SC) track overlap inefficiency in terms of $\Delta\phi_{SC} = |\phi(\pi^\pm) - \phi(\pi^\pm)|$, as illustrated in Fig. 14 (b): the angle between the lost track and the reconstructed track with the same charge. For data in Fig. 15(c) the angle between lost track and reconstructed track with the same charge in the 3-track sample is plotted in red. The blue histogram shows the same distribution for the two detected tracks. The distribution with one lost track is the superposition of the distribution due to detection inefficiency and a peaking distribution at small $\Delta\phi_{SC}$ due to track overlap losses. The distribution due to usual detection inefficiency has the same $\Delta\phi_{SC}$ dependence as the distribution of the two measured tracks. The number of tracks lost due to track overlap can be estimated by scaling down the distribu-

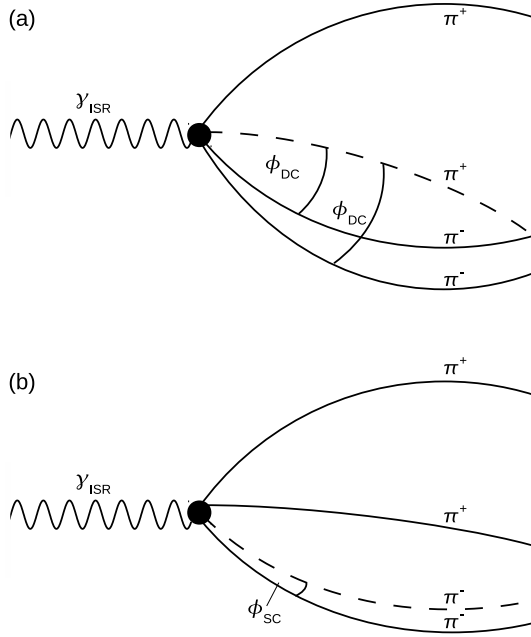


Figure 14: (a): Charge oriented azimuthal angle between missing pion and detected pions with different charge $\Delta\phi_{DC} = \phi(\pi^+) - \phi(\pi^-)$ (2 entries per event); (b) absolute value of azimuthal angle between missing pion and detected pion with same charge $\Delta\phi_{SC} = |\phi(\pi^\pm) - \phi(\pi^\pm)|$.

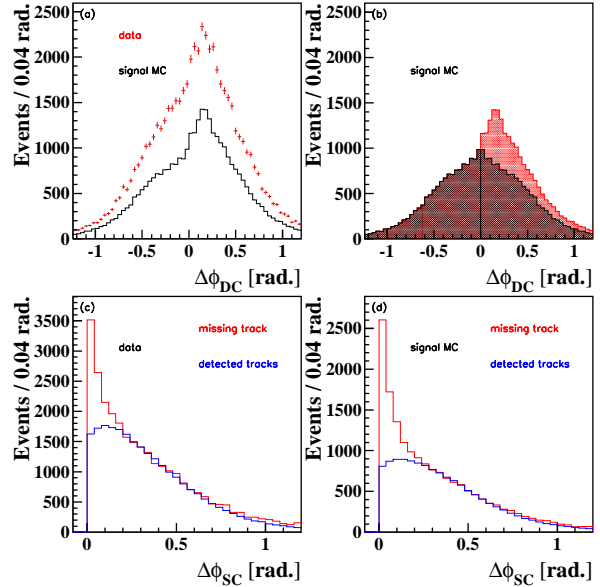


Figure 15: (a): Angle between missing pion and detected pions with different charge for the data (red points) and signal simulation normalized to the luminosity (black histogram). Two entries per event. (b): Illustration of the cleaning procedure. Tracks lost due to DC overlap (red) and due to other effects (black). (c): Angle between missing pion and detected pions with same charge (red) and the angle between two detected pions (blue) normalized to the same number of events in the region $0.3 \text{ rad} < \Delta\Phi < 0.8 \text{ rad}$. (d): Same as (c), but for signal MC.

tion of the measured tracks until the tails of the distribution match with the distribution including one missing pion. The difference at small $\Delta\phi_{SC}$ is a good estimate for the number of tracks lost due to track overlap. The corresponding distributions for MC are displayed in Fig. 15(d). The effect of SC tracks overlap is well modeled in MC.

5.4. ISR Efficiency Summary

To summarize, the difference in tracking inefficiency per track including track overlap is determined from ISR events to be:

$$\Delta\eta = (0.75 \pm 0.05_{stat} \pm 0.34_{syst})\% \quad (14)$$

Because of the track isolation requirement applied in the Tau31 selection, the different track multiplicity, and the different event topology, the ISR study includes a significantly higher track overlap probability and thus the value in equation 14 is not directly comparable with the Tau31 result discussed in Section 4. To make a comparison, we quantify the effect due to track overlap by studying the distributions of the azimuthal angular difference between same charged tracks and oppositely charged tracks. Taking this effect into account, we measure an efficiency difference between data and simulation of:

$$\Delta\eta' = (0.38 \pm 0.05_{stat} \pm 0.39_{syst})\% \quad (15)$$

This result is consistent with the Tau31 efficiency difference within the uncertainties. Depending on the event multiplicity and kinematics, *BABAR* analyses may need the inefficiency with or without track overlap effects.

6. Tracking Charge Asymmetry

Since a main objective of the *BABAR* experiment is to measure CP violation, it is vital to understand and measure any possible charge asymmetry in the track reconstruction. For instance, a promising mode for searching for CP violation in charm decays is $D^\pm \rightarrow K^+ K^- \pi^\pm$. An asymmetry in the reconstruction efficiency for the π^\pm would bias the CP result. Because the signal in these decays has a statistical uncertainty of $\sim 0.25\%$, a comparable control of the tracking efficiency asymmetry is needed.

We define the charged pion tracking asymmetry as

$$a(p_{Lab}) \equiv \frac{\epsilon(p_{\pi^+}) - \epsilon(p_{\pi^-})}{\epsilon(p_{\pi^+}) + \epsilon(p_{\pi^-})} \quad (16)$$

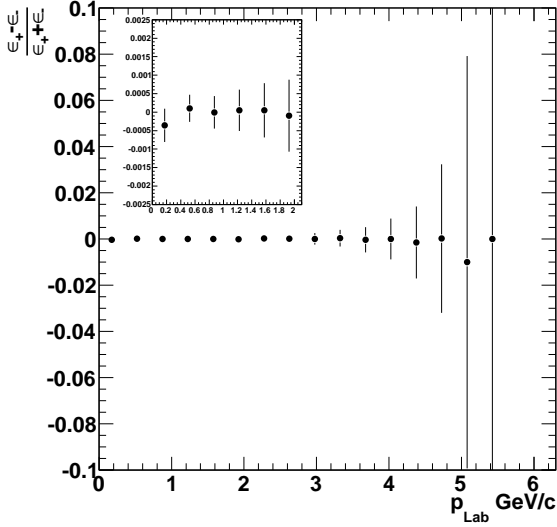


Figure 16: Tracking asymmetry from MC as a function of charged pion momentum in the laboratory frame. The inset plot shows the asymmetry up to 2 GeV.

674 where p_{Lab} indicates that momenta are in the lab frame,
 675 and p_{π^+} (p_{π^-}) refers to the momentum of the positively
 676 (negatively) charged pion.

677 We illustrate our expectations in this regard using
 678 MC. Figure 16 shows the pion tracking efficiency asym-
 679 metry derived from MC using generator information
 680 for pion tracks in $D^\pm \rightarrow K^+K^-\pi^\pm$ decays. The av-
 681 erage asymmetry for MC in this mode is found to be
 682 $a(p_{Lab}) = (-6 \pm 23) \times 10^{-5}$, consistent with zero within
 683 the uncertainties, and without any significant momen-
 684 tum dependence.

Two different methods are used to determine the pion
 track efficiency asymmetry directly from data. The
 more precise technique relies on Tau31 events. We work
 directly in the observed variables and use the ratios of
 the numbers of two-hadron decays to three-hadron de-
 cays to determine the pion inefficiency. Instead of fitting
 distributions of 2- and 3-hadron decays, we recognize
 that the (fewer) 2-hadron events that arise from track-
 ing inefficiency can be easily modeled directly from the
 3-hadron events. In practice this is done by weighting
 every 3-hadron event by the ratio $(1 - \epsilon)/\epsilon$, where ϵ
 is the track efficiency of the observed third track. For
 both 3-hadron as well as 2-hadron events we select only
 events from the ρ -decay channels $\tau^- \rightarrow \rho^0 h^- \nu_\tau$, ac-
 cording to the selection criteria described in section 4
 since the inclusive $\tau^- \rightarrow \pi^- \pi^- h^+ \nu_\tau$ has more signifi-
 cant backgrounds, specifically with contamination from

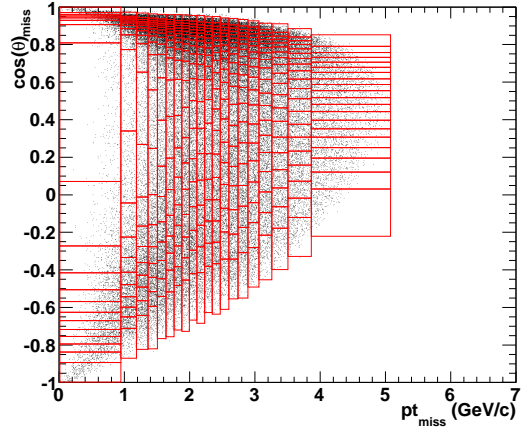


Figure 17: Distribution of the observed 2-hadron events for the full BABAR data sample. Bin boundaries were chosen to obtain the same number of events (215) in each bin.

electrons. The total number of 2-prong (3-prong) events
 in the sample is 86,092 (1,365,900). The distribution of
 events in the observed variables, pt_{miss} and $\cos(\theta)_{miss}$, is
 shown in Figure 17. The observed variables are deter-
 mined from the 2-prong momenta:

$$\vec{p}(\pi\pi) \equiv \vec{p}(\pi^+) + \vec{p}(\pi^-) \quad (17)$$

such that

$$\cos(\theta)_{miss} = \frac{p_z(\pi\pi)}{p(\pi\pi)} \quad (18)$$

and

$$pt_{miss} = p_T(\pi\pi). \quad (19)$$

In order to fit these event distributions, one must
 also account for backgrounds. The 2-hadron events of
 interest include approximately 7% background events.
 Chief among these are events from photon (5%) and
 π^0 (1%) conversions in 1-hadron decays of the tau,
 where the 1-prong track from the tau is combined with
 a track from the photon or π^0 and identified as a 2-prong
 event. Inelastic nuclear interactions due to tracks pass-
 ing through detector material and other backgrounds
 are small in comparison. The backgrounds are split
 into “photon” and “other” components and the overall
 normalization of each distribution is a parameter in a
 binned χ^2 fit. Another large background contribution to
 2-hadron events (whose normalization is a parameter) is
 acceptance loss events due to the third track being lost
 in the direction of the beam. PDFs are obtained from MC
 as normalized histograms in the observed variables of

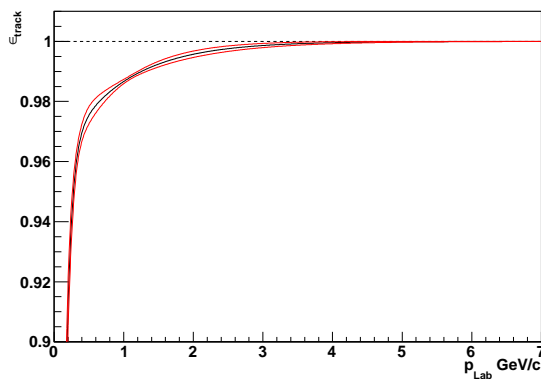
702 the various backgrounds; events in these have been re-
 703 weighted to account for inadequacies in the MC 3-body
 704 Dalitz distributions by matching the 3-body mass distri-
 705 bution as well as both the 2-body mass distributions to
 706 those in data. The tracking efficiency asymmetry fit is a
 707 binned χ^2 -fit with binning as shown in Fig. 17.

708 The significant parameters in the fit describe the
 709 tracking efficiency and the asymmetry as a function of
 710 the lab momentum. The tracking efficiency is param-
 711 eterized with the following phenomenological formula:

$$\epsilon(p_{Lab}) = 1 - A_0 e^{-\frac{p_{Lab}-p_0}{\tau_0}} - B_0 e^{-\frac{p_{Lab}-p_1}{\tau_1}} \quad (20)$$

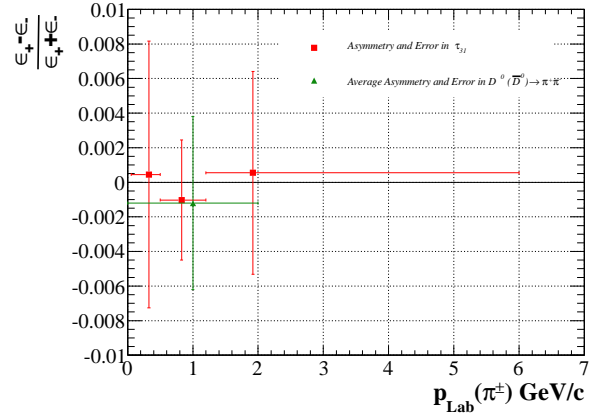
712 where the parameters are A_0 , B_0 , p_0 , p_1 , τ_0 , and τ_1 , in
 713 addition to parameters which measure the asymmetry in
 714 bins of lab momentum. Finally, it should be mentioned
 715 that we account for differences in the 3-hadron distri-
 716 butions of m_{12}^2 versus m_{23}^2 (1, 2, 3 denote the particles
 717 in the 3-prong tau decay) in data and MC by weighting
 718 3-hadron events according to the data/MC m_{12}^2 , m_{23}^2
 719 distribution ratio. The fit to our data is good as evidenced
 720 by a $\chi^2/NDF = 792/780$, i.e., a 37% probability.

721 Results from this procedure are shown in Figures 18
 722 and 19. We find the average charged pion tracking effi-
 723 ciency asymmetry to be $a(p_{Lab}) = (0.10 \pm 0.26)\%$, in our
 724 momentum range of approximately 0-4 GeV/c, consis-
 725 tent with zero. To account for systematic errors we re-fit
 726 the data with the following variations. We force the ac-
 727 ceptance loss and background descriptions in the fit in-
 728 dividually to be charge-independent, and we reduce the
 729 number of background components by combining some
 730 PDFs. We find the total systematic error to be 0.10%.



731 Figure 18: The tracking efficiency determined by the Tau31 method
 732 as a function of charged pion momentum in the laboratory frame. The
 733 red envelope around the efficiency curve indicates 1σ statistical error
 734 bands.

735 Another technique we use to measure the charged
 736 track efficiency asymmetry utilizes isotropy of spinless-



737 Figure 19: The tracking asymmetry determined by the Tau31 method
 738 as a function of charged pion momentum in the laboratory frame. The
 739 average asymmetry over momenta 0-2 GeV/c determined from D^0
 740 decays is also shown here for comparison.

741 two-body decays. In this method we study the $D^0 \rightarrow$
 742 $\pi^+\pi^-$ and $\bar{D}^0 \rightarrow \pi^+\pi^-$ decays. We require that these de-
 743 cays not be from B-meson decays (as these have larger
 744 backgrounds) and that they be tagged as being from $D^{*\pm}$
 745 decays to improve signal purity. Also, in both cases we
 746 require that at least one pion have momentum greater
 747 than 2 GeV/c and assume that the tracking efficiency
 748 charge asymmetry is zero for this pion. Therefore, any
 749 asymmetry in yields is the result of tracking asymmetry
 750 of the lower momentum pion which is reported below.

751 High purity samples of D^0 and \bar{D}^0 decays are ob-
 752 tained using slow pions associated with the decay of D^{*+}
 753 to tag the flavor of the D^0 meson. A detailed description
 754 of the event selection is described in the publication of
 755 $D^0 - \bar{D}^0$ mixing using the ratio of lifetimes for the decay
 756 of $D^0 \rightarrow \pi^+\pi^-$ [19]. Particle identification is not applied
 757 to the selection of pion tracks, rather we choose to re-
 758 move reflections from the $K^-\pi^+$ decays of the D^0 using
 759 a cut on the reflected mass and we account for the re-
 760 maining contamination from the tails by studying their
 761 $\pi^+\pi^-$ mass distributions and including a term with such
 762 a shape in our 1-D binned $\pi^+\pi^-$ mass fit. Yields of D^0
 decays where the higher momentum track is either the
 π^+ or the π^- are separately determined and are used to
 determine the asymmetry. A similar study is carried out
 using \bar{D}^0 decays, and the combined charge asymmetry
 of the efficiency, averaged over pion momenta from 0 to
 2 GeV/c is found to be $a(p_{Lab}) = (-0.12 \pm 0.50)\%$, con-
 sistent with zero and the Tau31 method result, but not
 as precise as the Tau31 method.

7. Low p_T tracking efficiency measurement

The τ pair sample provides an estimate of tracking efficiency for charged tracks with $p_T > 180$ MeV/c only. However, the detection of low p_T tracks ($p_T < 180$ MeV/c) is important for tagged D^0 analyses. D^0 tagging is performed through the $D^{*+} \rightarrow D^0 \pi^+$ decay, where the soft pion (π_s^+) is emitted with an energy just over its rest mass in the D^{*+} frame, and so typically has very low p_T in the lab frame. D^0 tagging is used in CP violation, mixing, and many other precision analyses, therefore a good understanding of the low p_T tracking efficiency is required.

The low p_T reconstruction efficiency analysis is based on a previous analysis by the CLEO collaboration [20]. CLEO demonstrated that the relative slow pion efficiency can be measured as a function of momentum using *helicity* distributions. The slow pion helicity angle θ^* is defined as the angle between the slow pion momentum in the D^* rest frame and the D^* momentum in the laboratory frame. This is illustrated in Fig. 20.

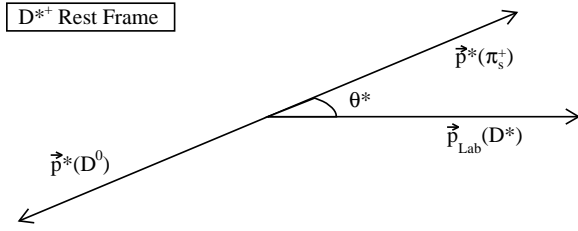


Figure 20: Definition of slow pion helicity angle θ^* .

When a vector meson decays to a final state made of two pseudo-scalar mesons, the distribution of the helicity angle is expected to be symmetrical and can be described as [21, 22]

$$\frac{dN}{d \cos \theta^*} \propto (1 + \alpha \cos^2 \theta^*), \quad 1 < \alpha < +\infty, \quad (21)$$

Furthermore, the cosine of the helicity angle is related to the slow pion momentum by:

$$p_{\pi_s} = \gamma(p_{\pi_s}^* \cos \theta^* - \beta E_{\pi_s}^*), \quad (22)$$

where β and γ are the D^* boost parameters. Since p^* and E^* are known once the D^* momentum is known, Eq. 22 maps any asymmetry observed in Eq. 21 to a relative reconstruction inefficiency in a specific part of the slow pion momentum spectrum.

We measure the $\cos \theta^*$ distribution in 8 bins of $p^*(D^*)$ spectrum as shown in Fig. 21. Since p_π depends not

just on the $\cos \theta^*$, but also on $p^*(D^*)$, we perform an angular efficiency analysis in bins of $p^*(D^*)$. We then fit these $\cos \theta^*$ distributions to a function defined as the convolution of Eq. 21 and the efficiency function:

$$\epsilon(p) = \begin{cases} 1 - \frac{1}{\delta(p-p_0)+1}, & \text{if } p > p_0 \\ 0, & \text{if } p \leq p_0. \end{cases} \quad (23)$$

The goal of this analysis is to compare data and MC efficiencies to get a systematic error from the relative difference between them:

$$\sigma_{syst} = \frac{\int \epsilon_{data}(p)dp - \int \epsilon_{MC}(p)dp}{\int \epsilon_{data}(p)dp}. \quad (24)$$

The limitations of this method are the effects that may be not correctly described in the MC, such as final state interactions or radiative losses.

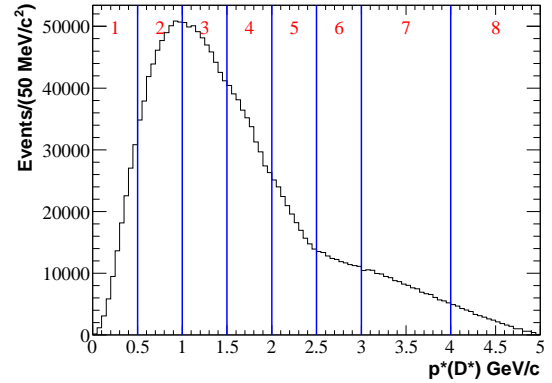


Figure 21: Distribution of $p^*(D^*)$ in the data sample. On top of the figure the blue lines show the lower and upper limit of each bin indicated by the red number.

The analysis is done using 470 fb^{-1} of data recorded by the BABAR detector and about 4.2×10^9 generic MC events. The decay chain $e^+e^- \rightarrow D^{*+} X$, $D^{*+} \rightarrow D^0 \pi_s^+$, $D^0 \rightarrow K^- \pi^+$ [23] is reconstructed in both data and MC, requiring particle identification for the kaon and the two vertices to be successfully reconstructed. The $D^0 \rightarrow K^- \pi^+$ mode is chosen to provide a clean sample of $D^{*+} \rightarrow D^0 \pi^+$ decays with a high branching fraction. A control sample is reconstructed the same way by not requiring the kaon identification. This sample is used for background subtraction. The $p^*(D^*)$ spectrum has been compared between data and MC. Differences are corrected for by weighting the MC sample which is then normalized to data.

As shown in Fig. 22, four categories of events can be recognized after the reconstruction:

- 813 1. signal: real D^0 and π_s^+ from D^{*+} decay. 844
- 814 2. Missed π_s^+ : real $D^0 \rightarrow K^- \pi^+$ decay that may or 845
815 may not have come from a D^{*+} , combined to a π^+ 846
816 from combinatoric. 847
- 817 3. Missed D^0 : a mis-reconstructed D^0 with a real π_s^+ 848
818 from D^{*+} . This is mostly $D^0 \rightarrow K^- K^+$, $D^0 \rightarrow K^-$ 849
819 $\pi^+ \pi^0$, $D^0 \rightarrow \pi^+ \pi^-$ or cases where the kaon and 850
820 pion assignments have been swapped. 851
- 821 4. Combinatoric background: neither D^0 or π_s^+ are 852
822 correctly reconstructed from a D^{*+} decay. 853

823 The amount of combinatoric and real D^0 , fake π_s^+ 854
824 background in the signal region is estimated using the 855
825 re-normalized distribution of the control sample D^0
826 sidebands in the $\Delta m = m(K^- \pi^+ \pi_s^+) - m(K^- \pi^+)$ signal
827 region. The scale factor needed for going from Δm side-
828 band to the Δm signal region is taken from the control
sample itself. This background subtraction procedure

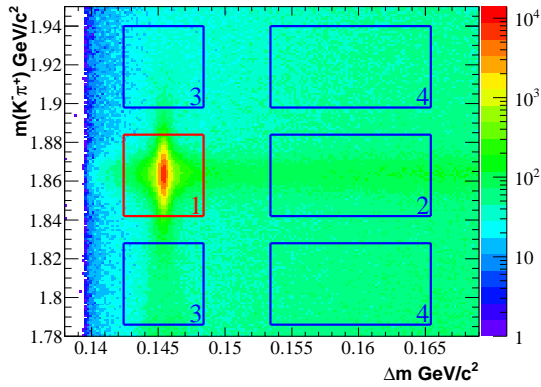


Figure 22: $m(K^- \pi^+)$ vs. Δm scatter plot of the data sample. Signal region is identified by the red box and the blue lines show the sidebands. The numbers identify the events category.

829 has been carried out for the $\cos \theta^*$ distribution for each
830 bin of $p^*(D^*)$ using the following steps:
831

- 832 1. consider the *no PID* sample in the $m(K^- \pi^+)$ side-
833 band regions; divide the number of events in the
834 Δm signal region by the number of events in the
835 Δm sideband to get the scale factor to go from side-
836 band to signal in Δm ;
- 837 2. in the *good PID* sample scale the $m(K^- \pi^+)$ spec-
838 trum in the Δm sideband region using the factor
839 obtained in the previous step; then integrate the
840 resulting $m(K^- \pi^+)$ spectrum to get the factor to
841 rescale background;
- 842 3. use the factor measured in step 2 to rescale
843 the interesting distribution ($\cos \theta^*$) obtained from

- 844 the events of the *no PID* sample in Δm signal,
845 $m(K^- \pi^+)$ sideband region (category 4);
- 846 4. subtract the distribution obtained in step 3 from the
847 same distribution retrieved from *good PID* sample
848 in signal region. 849

This procedure has been carried out for the $\cos \theta^*$ dis-
tribution for each bin of $p^*(D^*)$. All the histograms have
been then fit to the convolution of Eqs. 21 and 23 to de-
termine the parameters of the efficiency function p_0 and
 δ . Measuring p_0 and δ for data and MC, we can evaluate
the systematic error using Eq. 24. The fit makes use of
a global χ^2 defined as

$$\chi^2 = \sum_{l,k} \frac{(D_{lk} - S_{lk})^2}{\sigma_{D_{lk}}^2}, \quad (25)$$

where k is the index referring to one of the 8 $p^*(D^*)$
regions, l refers to one of the 16 bins of the $\cos \theta^*$ his-
togram in that region. D_{lk} , $\sigma_{D_{lk}}$ and S_{lk} are the number
of events observed in the bin, its error and the number
of events expect by the fit model, respectively. The ex-
pression of the fit model is

$$S_{lk} = \sum_{i,j} \epsilon(p_{ij}; p_0, \delta) N_k (1 + \alpha_k \cos \theta_i^*) \quad (26)$$

856 where i indicates the bin of the $\cos \theta^*$ distribution in the
857 k^{th} $p^*(D^*)$ region, and j is one of the 10 bins of the de-
858 tailed distribution within the range of momentum con-
859 sidered in the k^{th} $p^*(D^*)$ region.

860 The number of floating parameters in the fit are 18:
861 8 normalization factors N_i , 8 α_i (one for each bin) from
862 Eq. 21, and δ and p_0 from Eq. 23. The fit has been made
863 both to data and MC, giving the results shown in Fig. 23
864 and Tab. 2.

865 Finally, the efficiency functions are compared in
866 Fig. 25. Please note that these distributions include ac-
867 ceptance. The method shown herein does not allow to
868 disentangle the acceptance from the soft pion efficiency.
869 The systematic uncertainty estimated from Eq. 24 for
870 the low p_T tracks is $\sigma_{\text{sys}} = 1.54\%$.

871 8. K_S^0 reconstruction efficiency measurement

872 A significant number of analyses in *BABAR* involve the
873 reconstruction of the decay $K_S^0 \rightarrow \pi^+ \pi^-$, where the two
874 charged pions belong to the list CT of all reconstructed
875 tracks in the event. The track reconstruction efficiency
876 for charged tracks originating within 15 mm in XY from
877 the beam spot is studied by the other methods presented
878 earlier in the paper. However, most of the K_S^0 's decay

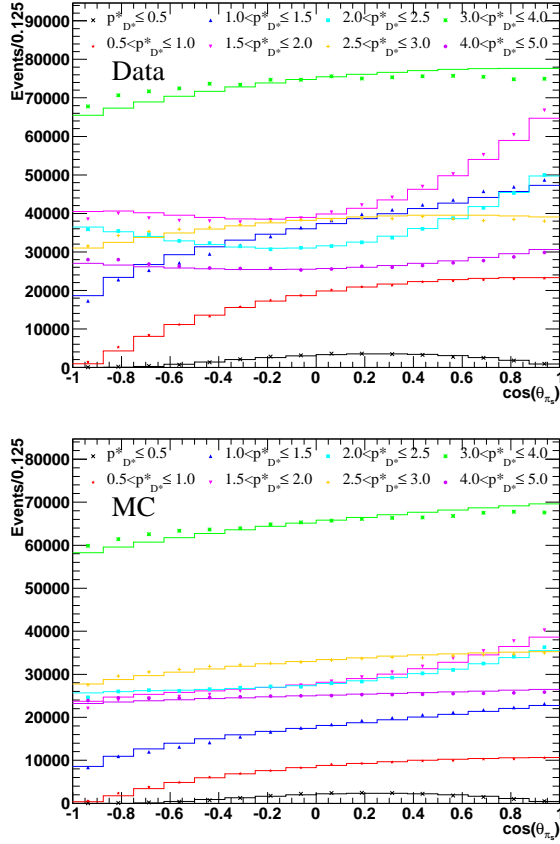


Figure 23: Fit of the model distribution to data (top) and MC (bottom). In both the plots, the measured data/MC event ratios are represented by the dots, while the fit results are shown using a line histogram. The distributions of $\cos \theta^*$ in the different ranges of $p^*(D^*)$ are shown using different colors, as outlined in the legend (the $p^*(D^*)$ values are measured in GeV/c). The fit to data returns $\chi^2/n_{dof} = 1.34$; the one to MC gives $\chi^2/n_{dof} = 0.71$.

879 outside this 15 mm radius, making it necessary to under-
 880 stand the K_S^0 daughter reconstruction efficiency in data and MC.
 881

882 The reconstruction efficiency of the K_S^0 daughters de-
 883 pends on the K_S^0 transverse momentum, p_T , polar angle,
 884 θ_{LAB} and transverse (XY) flight distance, d_{XY} , which is
 885 computed as the distance between the primary vertex of
 886 the event and the refitted K_S^0 decay vertex.

887 The general strategy is to subdivide the data and MC
 888 events into a large number of samples by choosing an
 889 appropriate binning in these variables, determine the
 890 number of K_S^0 's in each bin in data and MC and, for each
 891 of the momentum and polar angle ranges, normalize the
 892 ratio of its value in the first bin in d_{XY} , where all tracking
 893 effects are understood to 1.000 by definition, with no as-
 894 sociated error other than the systematic uncertainty per

Table 2: Fit results on data and MC.

Parameter	MC	Data
δ	13.77 ± 0.18	14.54 ± 0.15
p_0	$27.82 \pm 0.21 \text{ MeV}/c$	$27.01 \pm 0.14 \text{ MeV}/c$
N_1	1284645 ± 1784	185581 ± 1927
α_1	$-9.88 \pm 0.12 \times 10^{-1}$	$-9.30 \pm 0.10 \times 10^{-1}$
N_2	452849 ± 3524	970429 ± 5694
α_2	$-8.25 \pm 1.41 \times 10^{-2}$	$-9.75 \pm 0.86 \times 10^{-2}$
N_3	738162 ± 4631	1482799 ± 7329
α_3	$7.12 \pm 0.89 \times 10^{-2}$	$8.95 \pm 0.60 \times 10^{-2}$
N_4	1023973 ± 5400	1527424 ± 6434
α_4	$2.53 \pm 0.07 \times 10^{-1}$	$5.19 \pm 0.06 \times 10^{-2}$
N_5	894908 ± 4092	1093406 ± 4040
α_5	$1.90 \pm 0.06 \times 10^{-1}$	$5.13 \pm 0.07 \times 10^{-1}$
N_6	937073 ± 3729	1050245 ± 3390
α_6	$-1.93 \pm 0.49 \times 10^{-2}$	$-6.36 \pm 0.44 \times 10^{-2}$
N_7	1738326 ± 5687	1948264 ± 5116
α_7	$0.98 \pm 3.43 \times 10^{-3}$	$-2.78 \pm 0.32 \times 10^{-2}$
N_8	626949 ± 1881	665218 ± 1678
α_8	$1.46 \pm 0.55 \times 10^{-2}$	$1.73 \pm 0.06 \times 10^{-1}$

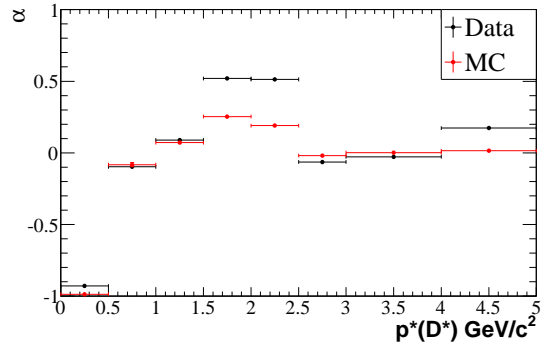


Figure 24: Comparison of the fit results on α in the 8 bins of $p^*(D^*)$ for data (black) and Monte Carlo (red). The difference observed in the 4th, 5th and 8th bins is due to the slightly different helicity distribution for data and MC in these $p^*(D^*)$ ranges.

895 track, as discussed in Section 4. Bin sizes are optimized
 896 to ensure a sufficient number of events in each bin, with
 897 4 bins in p_T (0.0 - 0.4 - 1.0 - 2.0 - 4.0 GeV/c), 8 bins in
 898 θ_{LAB} ($7.0^\circ - 25.6^\circ - 44.25^\circ - 62.88^\circ - 81.5^\circ - 100.13^\circ -$
 899 $118.75^\circ - 137.38^\circ - 156.0^\circ$) and 10 bins in d_{XY} (0.0 -
 900 0.3 - 1.3 - 2.78 - 3.2 - 4.0 - 5.4 - 9.1 - 11.4 - 23.6 - 40.0
 901 cm). The binning in d_{XY} roughly reflects the structure
 902 of the $BABAR$ detector and the bins are numbered from 0
 903 to 9, bin 1 being the normalization bin. The normalized
 904 ratio of the data and MC as a function of different bins
 905 is provided as a correction factor for the K_S^0 daughter
 906 reconstruction efficiency. In order to reduce the uncer-
 907 tainty from the imperfect simulation of the random track
 908 background or the potential differences between the K_S^0
 909 quality cut efficiencies in data and MC, we remove the

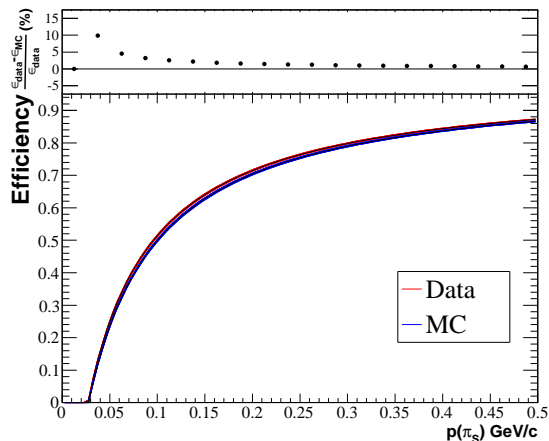


Figure 25: Soft pion reconstruction efficiency functions obtained from the fit to data (red) and MC (blue). Both the efficiency functions are shown together with the functions obtained by varying the central values of the fit parameters p_0 and δ by 1σ . The curve obtained using the central values is drawn in black. On top of the curves, the distribution of the relative difference between data and MC is shown.

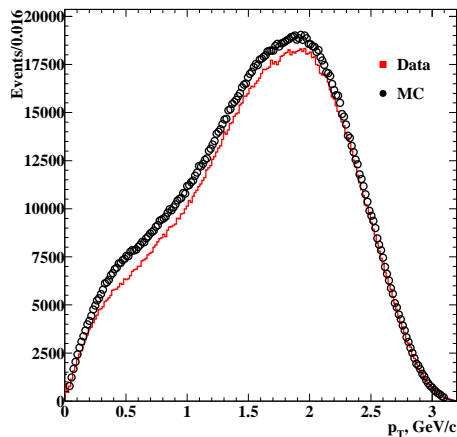
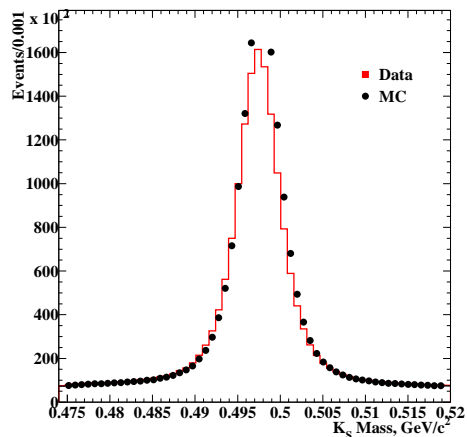


Figure 26: K_S^0 mass (top) and transverse momentum (bottom) for data and MC. MC is normalized to the data luminosity.

910 immediate vicinity of the event's primary vertex which
911 is 3 mm in XY from the first (normalization) bin.

912 Events of interest are selected by looking for the
913 $B \rightarrow h^+ h^- K_S^0$ (with $h = \pi, K$) decays in the data and
914 MC samples. The MC sample includes events from
915 generic B decays, light quark events (u,d,s,c) and $\tau^+ \tau^-$
916 decays. The K_S^0 is reconstructed from two oppositely
917 charged tracks, the invariant mass of which is required
918 to be within 25 MeV/c^2 of the PDG value of the K_S^0
919 mass ($m_{K_S^0} = 497.614 \pm 0.024 \text{ MeV}/c^2$) [6]. The two
920 oppositely charged tracks must originate from a common
921 vertex and the fit is required not to fail. The event is
922 required to have at least five GT tracks, two of which are
923 oppositely charged GT tracks that when combined with
924 the K_S^0 candidate to form an object with $m_{ES} > 5.19$
925 GeV/c^2 and $|\Delta E| < 0.3 \text{ GeV}$. About 93% of these events
926 come from the light quark (udsc) continuum; the
927 contribution from $\tau^+ \tau^-$ production is about 2.5% and only
928 about 3.5% of candidates arise from B decays, most of
929 which are random track combinations. Figures 26 and
930 27 show the data and MC comparison of the K_S^0 mass,
931 p_T , θ_{LAB} and d_{XY} distributions for the reconstructed K_S^0
932 candidates.

933 To determine the number of K_S^0 's in each of the bins
934 in data and MC, the K_S^0 mass distributions in each of
935 the bins are fitted with a sum of a double Gaussian and
936 a constant background. The constant background, deter-
937 mined from the sideband regions in the K_S^0 mass
938 distribution, $[0.476, 0.485] \cup [0.511, 0.520] \text{ GeV}/c^2$, for
939 each bin, is then subtracted to determine the number of

940 K_S^0 in each bin. The limited statistics in a large fraction
941 of bins makes it impractical to allow the slope of the
942 background to float. The binned maximum log likeli-
943 hood method is used since the default χ^2 -minimization
944 method is less appropriate in this study as it systemati-
945 cally, in a statistics-dependent way, underestimates the
946 number of events in each bin.

947 We define the values of the normalized ratios R_{ijk} and
948 the uncertainties $\sigma_{R_{ijk}}$, where the indices i, j and k stand
949 for the number of the p_T , θ_{LAB} and d_{XY} bins respectively,
950 to be

$$R_{ijk} = (N_{ijk}/M_{ijk})/(N_{ij1}/M_{ij1}) \quad (27)$$

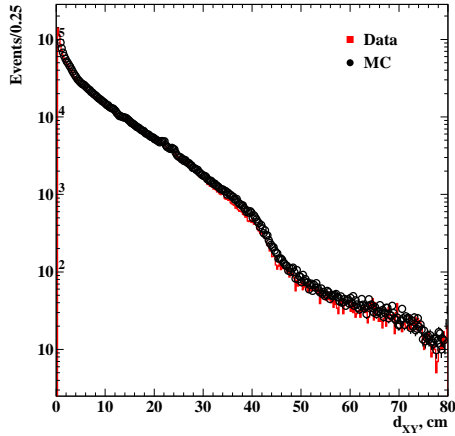
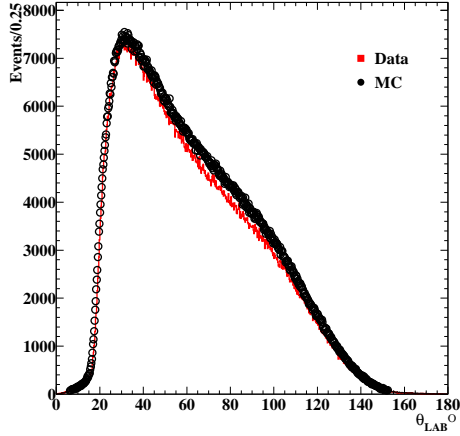


Figure 27: K_S^0 polar angle (top) and transverse flight length (bottom) for data and MC. MC is normalized to the data luminosity.

$$\sigma_{R_{ijk}} = R_{ijk} \sqrt{(\sigma_{N_{ijk}}/N_{ijk})^2 + (\sigma_{M_{ijk}}/M_{ijk})^2} \quad (28)$$

951 where N_{ijk} and $\sigma_{N_{ijk}}$ are the numbers of K_S^0 's and their
 952 uncertainties in data and M_{ijk} and $\sigma_{M_{ijk}}$ are the numbers
 953 of K_S^0 's and their uncertainties in MC. We also take into
 954 account the difference in the K_S^0 mass resolutions in data
 955 and MC by performing numerical integration to deter-
 956 mine the efficiencies of the $|m_{\pi^+\pi^-} - m_{K_S^0}| < 12 \text{ MeV}/c^2$
 957 cut in data and MC. The efficiency corrected normalized
 958 ratio, R_{ijk} , also called the correction factor, is computed
 959 for each bin and also as a function of several different
 960 sets of K_S^0 quality cuts (cuts on the K_S^0 mass, 3-D or XY
 961 flight length or its significance, the 3-D or XY angle,

962 α between the K_S^0 momentum and the line connecting
 963 the K_S^0 decay vertex and the primary vertex of the event,
 964 and, in one instance, a cut on the $K_S^0 \rightarrow \pi^+\pi^-$ vertexing
 965 quality), which also enables us to study the systematic
 966 uncertainties associated with a correction factor.

967 To get the overall correction in the K_S^0 daughter re-
 968 construction efficiency in an analysis, we apply the cor-
 969 rection factors to the signal MC. If H_{ijk} is the num-
 970 ber of events in the signal MC sample that falls within
 971 the bin (ijk), the relative weight of a K_S^0 reconstruc-
 972 tion efficiency correction table element R_{ijk} is $H_{ijk} /$
 973 H_{tot} , where $H_{tot} = \sum H_{ijk}$ and its statistical uncertainty is
 974 $\sqrt{(H_{ijk})/H_{tot}}$. The central value of the overall data/MC
 975 efficiency ratio is simply given by

$$R = \frac{1}{H_{tot}} \sum_{ijk} H_{ijk} C_{ijk} = \sum_{ijk} R_{ijk} C_{ijk} \quad (29)$$

976 Calculation of the statistical uncertainty on this num-
 977 ber is slightly non-trivial since we have to take into ac-
 978 count the fact that the statistical uncertainty on the nor-
 979 malization bin ratio, $\sigma_{R_{ijl}}$, influences the entire row (ij).
 980 Substituting R_{ijk} in Eq. 29 with the expression in Eq. 27
 981 and differentiating the resulting expression with respect
 982 to each of the variables that enter it while using $R_{ijl} =$
 983 1, we obtain

$$\sigma_R = \frac{1}{H_{tot}} \sum_{ij} \left\{ \sum_k H_{ijk} R_{ijk}^2 + \sum_{k \neq l} \{H_{ijk} \sigma_{R_{ijk}}\}^2 + \left\{ \sum_{k \neq l} H_{ijk} R_{ijk} \sigma_{R_{ijl}} \right\}^2 \right\}^{\frac{1}{2}} \quad (30)$$

984 where the first term reflects the finite size of the signal
 985 MC sample used in the study and is generally the small-
 986 est, the second term reflects the statistical uncertainties
 987 on the number of K_S^0 's in bins other than the normaliza-
 988 tion bin, and the third term, the dominant one, reflects
 989 the dependence on the statistical precision of R_{ijl} of the
 990 correction factors in each of the bins R_{ijk} , $k \neq l$.

991 The K_S^0 correction factors are applied to signal MC
 992 for the decay modes $B^0 \rightarrow \phi K_S^0$ and $B^0 \rightarrow \pi^+ D^-$ ($D^- \rightarrow$
 993 $K_S^0 \pi^-$), which provide K_S^0 spectra representative of most
 994 cases of K_S^0 used in *BABAR* analyses, to determine the
 995 overall correction factor and its statistical error. The
 996 above exercise is repeated for several sets of K_S^0 qual-
 997 ity cuts, from none to tight, and for three different bin-
 998 ning approaches. Half of the largest deviation in the K_S^0
 999 correction factors for different K_S^0 quality cuts is con-
 1000 sidered to be the systematic uncertainty associated with
 1001 K_S^0 daughter reconstruction efficiency. For these modes
 1002 we are able to determine the ratio of the data and MC

1003 K_S^0 daughter reconstruction efficiency to be about 99.5% 1050
1004 and with a statistical error of $\sim 0.4\%$ and a systematic 1051
1005 uncertainty of $\sim 0.7\%$. 1052

1006 9. Conclusion 1053

1007 In conclusion, we studied the track reconstruction 1054
1008 efficiency of charged particles in *BABAR* over a wide 1055
1009 range of momentum, polar angle, and track separation. 1056
1010 Our results come from several different control sam- 1057
1011 ples, which are observed to be self-consistent, and well 1058
1012 modeled in MC. The overall reconstruction efficiency 1059
1013 for isolated tracks is found to be consistent with MC 1060
1014 predictions. We also measured the charge asymmetry 1061
1015 in the track reconstruction, which was found be con- 1062
1016 sistent with zero. Any observed difference between 1063
1017 data and MC in the track reconstruction efficiency could 1064
1018 be considered as a source of systematic uncertainty in 1065
1019 all the physics analyses in *BABAR*. For physics anal- 1066
1020 yses with low multiplicity and similar topology to the 1067
1021 Tau31 decays and for charged tracks with momentum 1068
1022 greater than 180 MeV/c, the results from the Tau31 1069
1023 study should be used; for other B and D decays, the 1070
1024 results from the ISR study could be considered. For 1071
1025 charged tracks with momenta less than 180 MeV/c, an 1072
1026 additional systematic uncertainty of 1.54% per track 1073
1027 should be applied. The K_S^0 reconstruction efficiency in 1074
1028 data and MC is found to be a function of K_S^0 momentum, 1075
1029 polar angle and transverse flight distance, which needs 1076
1030 to be considered for K_S^0 reconstruction in *BABAR*. 1077

1031 10. Acknowledgements 1078

1032 We are grateful for the extraordinary contributions of 1079
1033 our PEP-II colleagues in achieving the excellent lumi- 1080
1034 nosity and machine conditions that have made this work 1081
1035 possible. The success of this project also relies criti- 1082
1036 cally on the expertise and dedication of the computing 1083
1037 organizations that support *BABAR*. The collaborating in- 1084
1038 stitutions wish to thank SLAC for its support and the 1085
1039 kind hospitality extended to them. This work is sup- 1086
1040 ported by the US Department of Energy and National 1087
1041 Science Foundation, the Natural Sciences and Engi- 1088
1042 neering Research Council (Canada), the Commissariat 1089
1043 à l'Énergie Atomique and Institut National de Physique 1090
1044 Nucléaire et de Physique des Particules (France), the 1091
1045 Bundesministerium für Bildung und Forschung and 1092
1046 Deutsche Forschungsgemeinschaft (Germany), the Isti- 1093
1047 tuto Nazionale di Fisica Nucleare (Italy), the Founda- 1094
1048 tion for Fundamental Research on Matter (The Nether- 1095
1049 lands), the Research Council of Norway, the Ministry of 1096

Education and Science of the Russian Federation, Min-
isterio de Ciencia e Innovación (Spain), and the Science
and Technology Facilities Council (United Kingdom).
Individuals have received support from the Marie-Curie
IEF program (European Union), the A. P. Sloan Founda-
tion (USA) and the Binational Science Foundation
(USA-Israel).

References

- [1] J. Sulkimo *et al.*, Nucl. Inst. and Meth. A **506** 250 (2003), J. Allison *et al.*, IEEE Trans. Nucl. Sci. **53** 270 (2006).
- [2] P. Golonka *et al.*, Comput. Phys. Commun. **174** 818 (2006), P. Golonka and Z. Was, Eur. Phys. J. C **45** 97 (2006).
- [3] D. J. Lange, Nucl. Instr. Methods Phys. Res., Sect. A **462**, 152 (2001).
- [4] B. Aubert *et al.* (*BABAR* Collaboration), Nucl. Instr. and Methods A **479**, 1 (2002).
- [5] D. Brown, talk presented at CHEP97, <http://www.ifh.de/CHEP97/abstract/a341.htm>.
- [6] K. Nakamura *et al.* (Particle Data Group), J. Phys. G **37**, 075021 (2010).
- [7] B. F. Ward, S. Jadach, and Z. Was, Nucl. Phys. Proc. Suppl. **116**, 73 (2003).
- [8] S. Jadach, Z. Was, R. Decker, and J. H. Kühn, Comp. Phys. Comm. **76**, 361 (1993).
- [9] E. Barberio and Z. Was, Comp. Phys. Comm. **79**, 291 (1994).
- [10] T. Sjostrand, Comput. Phys. Commun. **82**, 74 (1994).
- [11] S. Jadach and Z. Was, Comput. Phys. Commun. **85**, 453 (1995).
- [12] V.P.Druzhinin, <http://www.slac.stanford.edu/BFR00T/www/Physics/Tools/>
- [13] H. Czyż, J.H. Kühn, A. Grzelinska and J.H. Kühn, Phys. Rev. D **81**, 094014 (2010).
- [14] B. Aubert *et al.* (*BABAR* Collaboration), Phys. Rev. D **70**, 072004 (2004).
- [15] B. Aubert *et al.* (*BABAR* Collaboration), Phys. Rev. D **73**, 052003 (2006).
- [16] B. Aubert *et al.* (*BABAR* Collaboration), Phys. Rev. D **76**, 092005 (2007).
- [17] B. Aubert *et al.* (*BABAR* Collaboration), Phys. Rev. D **76**, 012008 (2007).
- [18] B. Aubert *et al.* (*BABAR* Collaboration), Phys. Rev. D **77**, 092002 (2008).
- [19] B. Aubert *et al.* (*BABAR* Collaboration), Phys. Rev. D **78**, 011105 (2008).
- [20] S. Menary, CLEO Internal Note, **CBX 92-103** (1992) (unpublished).
- [21] G. Brandenburg *et al.* (CLEO Collaboration), Phys. Rev. D **58**, 052003 (1998).
- [22] L. Gibbons *et al.* (CLEO Collaboration), Phys. Rev. D **56**, 3783 (1997).
- [23] Charge-conjugate reactions are implied throughout this paper except for section 6.